Journal of Molecular Structure: THEOCHEM 947 (2010) 1–8

Contents lists available at ScienceDirect

Journal of Molecular Structure: THEOCHEM

journal homepage: www.elsevier.com/locate/theochem

Static and dynamic reaction pathways involved in the reaction of O^- and CH_3F

Feng Yu, Lixia Wu, Shilin Liu, Xiaoguo Zhou *

Hefei National Laboratory for Physical Sciences at the Microscale, Department of Chemical Physics, University of Science and Technology of China, Hefei, Anhui 230026, China

ARTICLE INFO

Article history:
Received 30 October 2009
Received in revised form 1 February 2010
Accepted 9 February 2010
Available online 13 February 2010

Keywords:
Atomic oxygen radical anion (O^-)
Methyl fluoride (CH_3F)
Bimolecular nucleophilic substitution (S_N2)
Born–Oppenheimer molecular dynamics (BOMD)

ABSTRACT

The static and dynamic reaction pathways involved in the reaction between O^- and CH_3F have been investigated. A special attention has been paid to the S_N2 reaction channel, that the intrinsic reaction coordinate (IRC) calculation, one-dimensional relaxed potential energy scan, and Born–Oppenheimer molecular dynamics (BOMD) simulations have been performed, respectively. Both the forward IRC calculation and the relaxed potential energy scan from the $[O\cdots CH_3\cdots F]^-$ barrier show that the static reaction products are HF and CH_2O^-. However, the BOMD simulations initiated at this S_N2 barrier reveal two major dynamic reaction processes, which correspond to the products of $HF + CH_2O^-$ and the S_N2 reaction products of $F^- + CH_3O$, respectively. Although only 104 dynamic trajectories are calculated, the $HF + CH_2O^-$ production channel seems to be more dominant than the S_N2 pathway. However, the electron detachment process of CH_2O^- potentially causes its vanishing in experiments as an anionic product.

1. Introduction

The reactions involving methyl fluoride (CH_3F) have attracted much attention because of their important roles in atmospheric chemistry and combustion chemistry [1–7]. As CH_3F is a typical polar molecule, the reaction between CH_3F and a nucleophile probably undergoes a process of the bimolecular nucleophilic substitution (S_N2) reaction, e.g. $CH_3F + OH^- \rightarrow CH_3OH + F^-$ [8,9]. On the other hand, the atomic oxygen radical anion (O^-) is one of the most important chemical active negative ions. The reactions of O^- with many neutral molecules have been widely investigated and reviewed [10]. As indicated in the previous experimental studies [11–13], the reaction between O^- and CH_3F is very rapid and presents a characteristic of the multi-channel production. Tanaka et al. obtained a bimolecular reaction rate constant of 1.1×10^{-9} cm^3 $molecule^{-1}$ s^{-1} using a flowing afterglow apparatus with a quadrupole mass spectrometer, and a branching ratio of OH^- (98%), F^- (1%), and CHF^- (1%) were measured [11]. Dawson et al. employed a modified ion cyclotron resonance (ICR) mass spectrometer to study this reaction and acquired a branching ratio of OH^- (80%) and CHF^- (20%) [12]. Another experimental study with a selected ion flow tube (SIFT) operated at 300 K has been performed recently [13]. A reaction rate coefficient of 1.4×10^{-9} cm^3 $molecule^{-1}$ s^{-1} and a branching ratio of OH^- (68%), CHF^- (31%), and F^- (1%) have been reported [13]. Although similar qualitative reaction mechanisms have been deduced from the observed anionic products in these experimental studies, the measured branching ratios have an obvious difference and demonstrate dependences of experimental conditions and ion detection techniques. A possible potential reason for the difference of the experimental branching ratios is that the secondary reactions of anionic products involved in the previous experiments cause contamination of the measured anions [10]. In principle, internal energy distributions of the anionic products can be used to distinguish them generated from the initial or secondary reactions, however, the corresponding measurements have not been performed in the previous experiments. More significantly, since the mass spectrometry cannot detect neutral products, the reaction process involving the electron detachment of anionic product cannot be identified in the experiments. Therefore, to obtain a comprehensive reaction mechanism of the title reaction, more extended experimental investigations are expected, while the theoretical calculations are believed to be more powerful to describe the details of reaction processes, especially when the secondary reactions and electron detachment processes exist.

Recently, Yamamoto et al. [7] theoretically studied three thermodynamic production pathways of the title reaction as follows,

$$\begin{aligned} O^- + CH_3F &\rightarrow F^- + CH_3O \\ &\rightarrow OH^- + CH_2F \\ &\rightarrow CHF^- + H_2O \end{aligned}$$

where these three reaction pathways were defined as S_N2 reaction channel, H abstraction channel and H_2O production channel, respectively. Based on the optimized intermediate complexes and transition states on the reaction potential energy surface (PES) with density functional theory (DFT), they presented a qualitative description of the reaction mechanism. For the S_N2 reaction chan-

* Corresponding author. Tel.: +86 551 3600031; fax: +86 551 3602323.
E-mail address: xzhou@ustc.edu.cn (X. Zhou).

0166-1280/$ - see front matter © 2010 Elsevier B.V. All rights reserved.
doi:10.1016/j.theochem.2010.02.008

nel, geometries of the reactant-like complex ($O^-\cdots CH_3F$), transition state ($[O\cdots CH_3\cdots F]^-$), and product-like complex ($CH_3O\cdots F^-$) were optimized with the C_s symmetry. However, the reported product-like complex ($CH_3O\cdots F^-$) was not a true minimum because of its imaginary vibrational frequency, and thus the nearby exit-channel PES needs to be further explored to confirm this S_N2 reaction process. Moreover, on the reaction PES obtained by Yamamoto et al. [7], the same intermediate complex and the same subsequent rate-controlling barrier for both the H abstraction and H_2O production channels were found. Based on this potential energy diagram, it is very hard to evaluate the dominant products in the $OH^- + CH_2F$ and $CHF^- + H_2O$ channels by employing the Rice–Ramsperger–Kassel–Marcus (RRKM) theory [14]. As suggested by Hase [8,15], only investigating the static reaction pathway and using the statistical theory like RRKM would not be sufficient in this case. Therefore, the reaction mechanism at the microscopic level should be investigated by following the dynamic reaction pathway, especially for the S_N2 reaction process.

In this work, we explore the static and dynamic reaction pathways with B3LYP [16,17] method for the S_N2 reaction channel. The forward intrinsic reaction coordinate (IRC) [18,19] calculation of the $[O\cdots CH_3\cdots F]^-$ transition state is performed to identify the linked product-like complex, while a relaxed potential energy scan from this barrier along the elongation of the C···F distance with other coordinates optimized is used to find the final products as well. Based on these calculations, we obtain a comprehensive description of the static reaction pathway after passing the S_N2 transition state. For comparison with the static reaction pathway, the Born–Oppenheimer molecular dynamics (BOMD) simulations [20–22] initiated at the $[O\cdots CH_3\cdots F]^-$ barrier are performed to present the dynamic effect on this process and reveal the dynamic reaction pathways on the exit-channel PES. On the other hand, as mentioned above, the H abstraction and H_2O production reaction processes undergo the same intermediate complex and the same transition state corresponding to the barrier of O^- attacking the H atom of CH_3F ($[O\cdots H\cdots CH_2F]^-$) [7], a preliminary BOMD simulation initiated at this barrier is carried out to show the dominant products and the dynamic reaction processes. As a result, a more reasonable reaction mechanism is elucidated and an animated dynamic image of the title reaction is displayed. In addition, we also compare the dynamic effect of this S_N2 reaction channel with the $OH^- + CH_3F$ reactive system [8], and thereby the coupling interaction between the transition vector (imaginary vibrational mode) and other vibrational modes is expected to be understood deeply, which is another motivation for us to reinvestigate the S_N2 reaction channel of the title reaction.

2. Computational methods

All the quantum chemical calculations and dynamic trajectory simulations are carried out with the Gaussian 03 program package [23]. In order to overcome convergence difficulties of the self-consistent-field (SCF) procedure in this open-shell reaction system, the quadratically convergent SCF method [24] has been applied (Appendix A. Supplementary material).

As mentioned above, the IRC calculation and relaxed potential energy scan are used, respectively, to describe the static reaction pathway, while the dynamic trajectory calculations on the exit-channel PES are performed with the BOMD method. Briefly, the trajectories are integrated by utilizing the Hessian-based predictor–corrector algorithm with Hessian updating for five steps on the Born–Oppenheimer PES calculated at the B3LYP/6-31+G(d,p) level of theory [25,26]. The step size for all the trajectories is set as the default value, 0.25 $amu^{1/2}$ bohr. The trajectories will be stopped once the centers of mass (CM) of the dissociating fragments are separated from 15 bohr or the overall steps exceed the maximal point.

Specifically, for the S_N2 barrier of $[O\cdots CH_3\cdots F]^-$, the mass-weighted internal coordinate IRC calculation has been performed at the B3LYP/6-31+G(d,p) level of theory, and the potential minima on both forward and reverse reaction directions have been identified, respectively. For comparison, one-dimensional relaxed potential energy scan at the B3LYP/6-31+G(d,p) level has been done along the elongation of the C···F distance with other coordinates optimized from the S_N2 barrier to show the corresponding products on the exit-channel PES, where the C···F distance is scanned from 1.744 Å to 7.744 Å with a step of 0.05 Å. Furthermore, accurate energies are also calculated at the G3MP2 [27] and CCSD(T) [28] levels of theory for the stationary points on the PES of the S_N2 reaction channel. The corresponding scaling factors for the zero-point energies (ZPEs) are taken from Ref. [29].

In dynamic trajectory calculations, the trajectories are initiated at the S_N2 transition state of $[O\cdots CH_3\cdots F]^-$. Starting conditions are determined by thermal sampling and microcanonical normal mode sampling [30,31]. For the thermal sampling, both the vibrational and rotational sampling temperatures are chosen as the previous experimental temperature of 300 K. The transition vector is set to point to the corresponding products, and the energy added to this imaginary vibrational mode is sampled from thermal distribution at 300 K and/or set to be 0.6 kcal/mol. For the microcanonical normal mode sampling, a total energy of 10 kcal/mol is randomly distributed into the transition vector and all other vibrational modes of the transition state, while the rotational sampling temperature is set to be 300 K as well. A total of 104 trajectories have been calculated for the thermal sampling and microcanonical normal mode sampling for the $[O\cdots CH_3\cdots F]^-$ transition state, and the maximal steps are specified to be 3500 for each trajectory. In these 104 trajectories, the total energies drift within a range of 0.001–1.025 kcal/mol, and the total angular momentums float within about 10^{-9}–10^{-7} ħ. In addition, to present the dynamic processes for the H abstraction and H_2O production reaction pathways, a total of 61 trajectories are calculated from the corresponding transition state of $[O\cdots H\cdots CH_2F]^-$ with the thermal sampling at 300 K, in which the maximal steps are specified to be 5000. The transition vector is set to point to the corresponding products, and the energy added to this imaginary vibrational mode is sampled from thermal distribution at 300 K. Among these 61 trajectories, the total energies of 57 trajectories drift within a range from 0.039 kcal/mol to 1.751 kcal/mol, and the total energies of the other four trajectories drift beyond 2 kcal/mol. The total angular momentums for these 61 trajectories float within about 10^{-8}–10^{-7} ħ.

Generally, at least 1000 trajectories are necessary to calculate branching ratios for a multi-channel reaction, which will cost too much to be completed here. Because the major aim of this study is to compare the static and dynamic reaction processes of the title reaction, we have only calculated the limited number dynamic trajectories initiated at the $[O\cdots CH_3\cdots F]^-$ and $[O\cdots H\cdots CH_2F]^-$ barriers. Although the number of trajectories is not sufficient to quantitatively calculate the branching ratios, it is very important for us to present dynamic effect on the reaction processes and reveal the final products, which are probably different from those of the static reaction pathways. As indicated in our calculations, an obvious dynamic effect has been found on the S_N2 exit-channel PES of the title reaction from the calculated 104 trajectories. Therefore, the balance between the computational cost and qualitative conclusion seems to be satisfied for our aims. It should be noted here that the convergence problem of the SCF procedure prevents us from modeling collision dynamics between O^- and CH_3F on the entrance-channel PES, and thus we pay our attention on the molecular dynamics on the exit-channel PES.

3. Results and discussion

3.1. Static reaction pathways from the $[O\cdots CH_3\cdots F]^-$ barrier revealed by the IRC calculation and one-dimensional relaxed potential energy scan

On the reaction PES calculated by Yamamoto et al. [7], the static reaction pathway for the S_N2 channel of O^- with CH_3F has been viewed as follows. At the beginning, O^- attacks C atom of CH_3F to form $O^-\cdots CH_3F$ complex (with C_s or C_{3v} symmetry), which is an energetic intermediate with an ability to overcome the subsequent S_N2 barrier, $[O\cdots CH_3\cdots F]^-$ (with C_s symmetry, close to C_{3v} symmetry). After passing the $[O\cdots CH_3\cdots F]^-$ barrier, another complex of $F^-\cdots CH_3O$ (with C_s symmetry) has been suggested to produce, which can ultimately decompose to F^- and CH_3O. However, the $F^-\cdots CH_3O$ complex on the exit-channel PES reported in their work has an imaginary frequency, indicating that it is not a true minimum. Thus, the reaction process of the S_N2 channel has only been presented partially in previous theoretical study [7]. To describe this S_N2 reaction pathway completely, the true product-like complex on the exit-channel PES should be identified.

The minimum energy path (MEP) of the S_N2 reaction channel has been calculated and shown in Fig. 1(a), and the corresponding major bond lengths and bond angle have been presented in Fig. 1(b). As shown in Fig. 1(a), the reverse IRC calculation for the $[O\cdots CH_3\cdots F]^-$ barrier points to a potential minimum denoted as

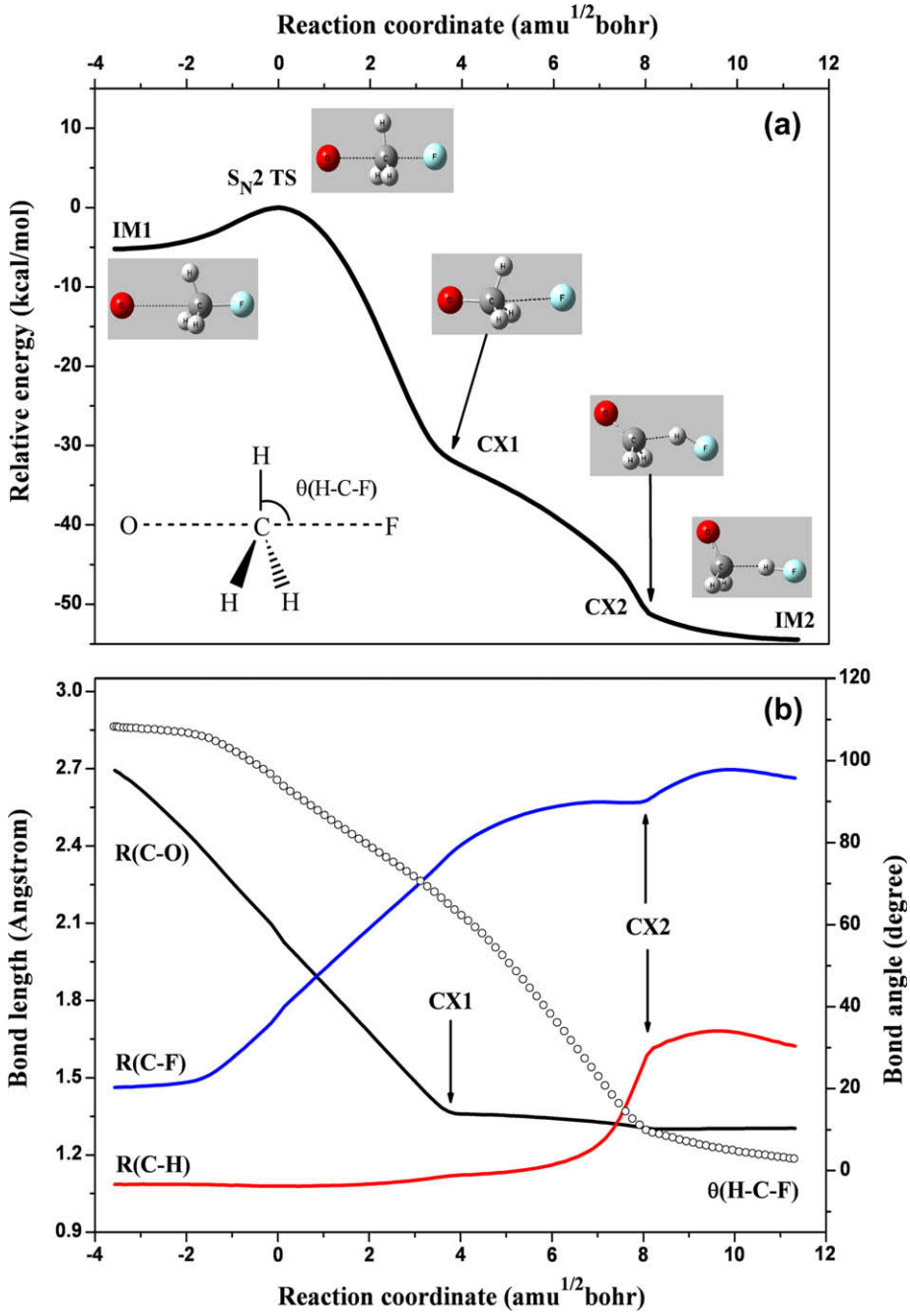

Fig. 1. The minimum energy pathway (MEP) for the S_N2 transition state of $[O\cdots CH_3\cdots F]^-$, the corresponding major bond lengths and bond angle along the MEP are shown, respectively. (a) The forward and reverse IRC profile, where the reverse minimum is the IM1 while the forward minimum corresponds to IM2, and two key complexes of CX1 and CX2 on MEP are noted as well. (b) The C–O bond length (in black), C–F distance (in blue), C–H bond length (in red) are presented with the solid lines, while the H–C–F bond angle are shown with the hollow circles. (For interpretation of the references to colour in this figure legend, the reader is referred to the web version of this article.)

IM1 on the entrance-channel PES. The IM1 is an ion–dipole intermediate complex formed by the collision of O^- with CH_3F, based on the geometry and Mulliken charge population analysis [32]. The forward IRC calculation leads to another potential minimum denoted as IM2 on the exit-channel PES. On the MEP along the forward IRC, the $[O\cdots CH_3\cdots F]^-$ barrier isomerizes to a special complex denoted as CX1 at the first stage, and the C···F distance is elongated as well as the C···O bond is formed simultaneously. As indicated in Fig. 1(a), the CX1 is an unstable complex, and the F^- of the CX1 can turn around and subsequently approach the H atom of CH_3O moiety to form the IM2 ultimately via another unstable complex CX2. Both the optimized molecular geometry and Mulliken charge population analysis of the IM2 demonstrate that it is indeed an ion–dipole intermediate complex formed by HF and CH_2O^-, which can subsequently decompose to HF and CH_2O^- since the overall energy of the products, HF and CH_2O^-, is much lower than that of the initial reactants, $O^- + CH_3F$. Obviously, the IM2 is not the typical product-like complex of the S_N2 reaction channel, therefore, it seems that the reaction does not proceed all through along the classical S_N2 pathway after passing the $[O\cdots CH_3\cdots F]^-$ barrier. However, no other stationary point without imaginary frequency has been found on the exit-channel PES. It should be noticed that the reaction stage of CX1 → IM2 is very similar to the "roaming" mechanism observed in the photodissociation of H_2CO [33,34], in which the dissociating H atom can turn around back to attract the H atom of HCO fragment and form the final product of $CO + H_2$. The similar roaming mechanism has also been observed in the dissociation of CH_3CHO [35].

Although both the molecular structure and Mulliken charge population of the CX1 indicate that it is very like the expected product-like complex of the S_N2 channel, the CX1 is an unstable complex of $F^-\cdots CH_3O$. Therefore, based on the MEP in Fig. 1(a), a reasonable supposition of the static reaction pathway is concluded as that the reaction initially proceeds along the S_N2 pathway to produce the CX1 after passing the $[O\cdots CH_3\cdots F]^-$ barrier, and then the unstable CX1 undergoes along the MEP to form the IM2, which can finally decompose to HF and CH_2O^-. The second stage of CX1 → IM2 makes the overall reaction process depart from the classical S_N2 reaction pathway.

Since the optimized distance between C and F atoms in the $[O\cdots CH_3\cdots F]^-$ barrier is 1.744 Å at the B3LYP/6-31+G(d,p) level, the relaxed potential energy curve along the elongation of the C···F distance for the $[O\cdots CH_3\cdots F]^-$ barrier has been calculated with other coordinates optimized from 1.744 Å to 7.744 Å and shown in Fig. 2 (solid line). With the elongation of the C···F distance, potential energy of the reactive system initiated from the $[O\cdots CH_3\cdots F]^-$ barrier quickly drops to a minimum similar to IM2 when the C···F distance is increased to 2.644 Å. Then the molecule dissociates to the final products of HF and CH_2O^- with the C···F distance further increased. Interestingly, if the corresponding C–H bond of the $[O\cdots CH_3\cdots F]^-$ barrier is frozen while scanning the relaxed potential energy, the potential energy curve will point to the expected products of the S_N2 channel, F^- and CH_3O, as the dotted line shown in Fig. 2. Thus, the one-dimensional relaxed potential energy scans show the consistent conclusion on the static S_N2 reaction process.

It is generally believed that the B3LYP method always underestimates the barrier heights, especially for the S_N2 reactions [36,37]. Therefore, we have calculated more accurate G3MP2 and CCSD(T) energies for the stationary points on the PES for the S_N2 reaction channel. As listed in Table 1, the B3LYP/6-31+G(d,p) level of theory underestimates the S_N2 barrier height within about 3 –4 kcal/mol. However, according to our calculations, the B3LYP/6-31+G(d,p) level of theory could characterize the exit-channel PES for this S_N2 reaction channel, and thus we choose this level to perform trajectory calculations. More significantly, the main purpose of this study is to present the dynamic effect rather than to quantitatively calculate the branching ratios, therefore a certain degree of the underestimated barrier height will not cause serious mistakes.

3.2. Dynamic reaction pathways revealed by the BOMD simulations initiated at the $[O\cdots CH_3\cdots F]^-$ barrier on the exit-channel PES

To study the dynamic reaction pathways after passing the $[O\cdots CH_3\cdots F]^-$ barrier, a total of 35 trajectories have been calcu-

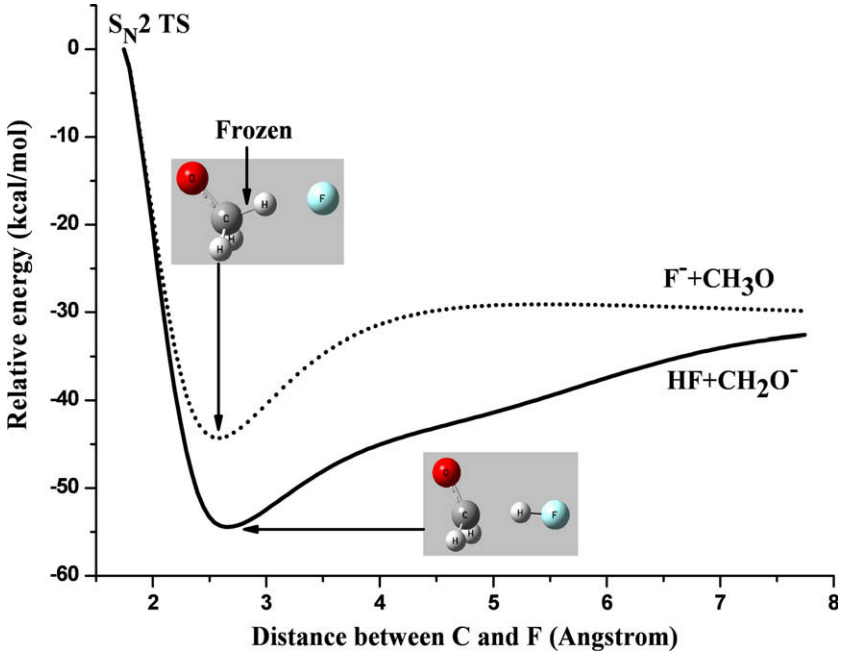

Fig. 2. Relaxed potential energy curve along the elongation of the C···F distance for the $[O\cdots CH_3\cdots F]^-$ barrier with other coordinates optimized is shown with solid line, while the dotted line presents the relaxed potential energy curve along the elongation of the C···F distance for this barrier with other coordinates optimized except the broken C–H bond frozen additionally.

Table 1
Energies for the stationary points on the PES for the S_N2 channel of O^- with CH_3F (kcal/mol).

Species	B3LYP[a]	G3MP2[b]	CCSD(T)[c]
$O^- + CH_3F$	0.0	0.0	0.0
$O^-\cdots CH_3F$ (IM1)	−13.0	−13.9	−12.8
$[O\cdots CH_3\cdots F]^-$ (S_N2 TS)	−8.4	−6.0	−4.3
$HF\cdots CH2O^-$ (IM2)	−64.5	−66.0	−63.8
$F^- + CH_3O$	−27.2	−26.6	−24.1
$HF + CH_2O^-$	−41.0	−46.2	−43.9

[a] Calculated at the B3LYP/6-31+G(d,p) level of theory, and the scaling factor for the ZPEs is 0.9806 [29].
[b] Computed based on the molecular geometries and ZPEs at the MP2(full)/6-31+G(d,p) level of theory. The PMP2 single-point energies have been used, and the scaling factor for the ZPEs is 0.9661 [29].
[c] Obtained at the CCSD(T,FC)/6-311++G(3df,2p)/MP2(FC)/6-31+G(d,p) level of theory, and the scaling factor for the ZPEs at the MP2(FC)/6-31+G(d,p) level of theory is 0.9608 [29].

lated via the BOMD simulations initiated at this barrier with the thermal sampling at 300 K, where the energy added on the transition vector is also sampled from the thermal distribution at 300 K. Two major types of dynamic reaction processes have been revealed by these 35 trajectories. The most major dynamic reaction pathway can be viewed as that the $[O\cdots CH_3\cdots F]^-$ barrier decomposes to the products of HF and CH_2O^-within a reaction time range between 254 fs and 2270 fs. Twenty three trajectories are of this type in all the calculated dynamic reaction pathways. The potential energy profiles for two typical trajectories of this type leading to HF and CH_2O^- are presented in Fig. 3. The first trajectory shows that the reactive system dissociates quickly to the products as displayed in Fig. 3(a), while the other shown in Fig. 3(b) corresponds to form the $HF\cdots CH_2O^-$ intermediate complex for a period of time and then dissociate. Interestingly, the case in Fig. 3(b) looks very like the "roaming" mechanism in dissociation of H_2CO [33,34] and CH_3CHO [35].

The second significant dynamic reaction pathway is found very similar to the classical S_N2 reaction channel, in which the $[O\cdots CH_3\cdots F]^-$ barrier directly dissociates to the S_N2 products of F^- and CH_3O within a short time range from 319 fs to 710 fs. Six trajectories are found to be of this type in the overall 35 trajectories. In Fig. 4, we present a potential energy profile along one of these trajectories, and molecular structures at several important reaction times are shown as well. Obviously, the unstable complex CX3 in Fig. 4 seems very similar to the CX1 at 3.890 $amu^{1/2}$ bohr in Fig. 1(a), indicating that the CX1 can dissociate directly to the S_N2 products of F^- and CH_3O, as we have suspected in the aforementioned static reaction pathway. Besides these two types, there are other dynamic reaction pathways with small possibilities. Three trajectories lead to H atom and $F^-\cdots CH_2O$ intermediate complex as products, while one trajectory corresponds to the final products of $F^- + CHO + H_2$. Actually, the $F^- + CHO + H_2$ production channel has been proposed as a possible production pathway by Peverall et al. [13], however, it has not been included in the previous theoretical work [7]. The present trajectory calculations confirm their surmise although the branching ratio of this channel seems very small. Moreover, in the calculated 35 trajectories, two trajectories stop at the $HF\cdots CH_2O^-$ intermediate complex within limited maximal steps, which will also ultimately produce the HF and CH_2O^- as products.

As the energy added on the transition vector is set to be 0.6 kcal/mol, and the vibrational and rotational degrees of freedom are sampled from the thermal distributions at 300 K, a total of 35 trajectories have been obtained. Among these 35 trajectories, 26 trajectories lead to HF and CH_2O^- as final products within a reaction time range from 303 fs to 2355 fs, and seven of them correspond to the S_N2 products of F^- and CH_3O within a short reaction time range between 233 fs and 534 fs. The other two trajectories lead to $F^-\cdots CHO + H_2$ and $HF\cdots CH_2O^-$ intermediate complex, respectively.

For the microcanonical normal mode sampling with 10 kcal/mol, a total of 34 trajectories have been calculated, and the obtained results are similar to the simulations with the thermal sampling mode. Two major dynamic reaction pathways have been presented among these 34 trajectories. The dominant dynamic reaction pathway with 14 trajectories shows the corresponding products of HF and CH_2O^- within a wide time range from 222 fs to 1516 fs, in which a fast dissociation process and a slow process with formation of the $HF\cdots CH_2O^-$ intermediate complex are identified, respectively. The other significant reaction pathway including eight trajectories leads to the F^- and CH_3O as products within a time range between 230 fs and 556 fs. Besides these 22 trajectories mentioned above, the other 12 trajectories correspond to the dynamic reaction pathways with small branching ratios, such as the $F^-\cdots CH_2O + H$, $F^- + CHO + H_2$, and $HF + CO^- + H_2$ production channels.

To be summarized, two major dynamic reaction pathways after passing the $[O\cdots CH_3\cdots F]^-$ barrier have been revealed by the BOMD simulations. The one leads to the products of HF and CH_2O^- (63/104, ~61%) and the other corresponds to F^- and CH_3O (21/104, ~20%). However, as the expected major anionic product in the present dynamic trajectory calculations, the CH_2O^- was not observed in the previous experiments [11–13], while the F^- was detected with a very small branching ratio [11,13]. A potential reason seems to be reasonable that the CH_2O^- is a temporary and unstable anion. According to the experimental study and quantum chemistry calculations [38–43], the electron affinity (EA) of CH_2O is negative, and thus the neutral formaldehyde molecule (CH_2O) will be produced in experiment through electron detachment of the CH_2O^-. Therefore, the previous experiments have not observed the CH_2O^- as an anionic product.

3.3. Driven energies for the major dynamic reactions pathways initiated at the $[O\cdots CH_3\cdots F]^-$ barrier on the exit-channel PES

There are two main cases in the dynamic trajectory simulations for the $[O\cdots CH_3\cdots F]^-$ barrier, when the kinetic energy is added on the transition vector. One is beneficial to the separation of F^- from CH_3O, when the coupling between the transition vector and other vibrational modes is weak and the intramolecular vibrational redistribution (IVR) [44,45] is not efficient. This dynamic behavior helps the title reactive system undergo the S_N2 reaction pathway to produce the F^- and CH_3O. It seems very similar to that of the $OH^- + CH_3F$ reactive system [8], in which "the very weak coupling between $CH_3OH + F^-$ relative translation and $O–C\cdots F^-$ bending and other vibrational degrees of freedom of the reactive system" makes most (~90%) of the trajectories initiated at the $[HO\cdots CH_3\cdots F]^-$ barrier directly dissociate to CH_3OH and F^- without trapping in the $CH_3OH\cdots F^-$ intermediate complex. The other case is exactly the opposite. When the coupling between the transition vector and other vibrational modes is relatively strong and the IVR is efficient, the strong interaction between F^- and CH_3O on the exit-channel PES will prevent F^- from departure and pull it back to interact with CH_3O moiety to ultimately produce HF and CH_2O^-.

In the title reaction, as mentioned above, the dynamic reaction pathway leading to the products of HF and CH_2O^- is relatively major, while the dynamic reaction pathway corresponding to the S_N2 products of F^- and CH_3O is relatively minor. This implies that the coupling between the transition vector and other vibrational modes of the $[O\cdots CH_3\cdots F]^-$ barrier is strong based on the current BOMD simulations at the B3LYP/6-31+G(d,p) level of theory. Furthermore, the occurrence of other dynamic reaction pathways,

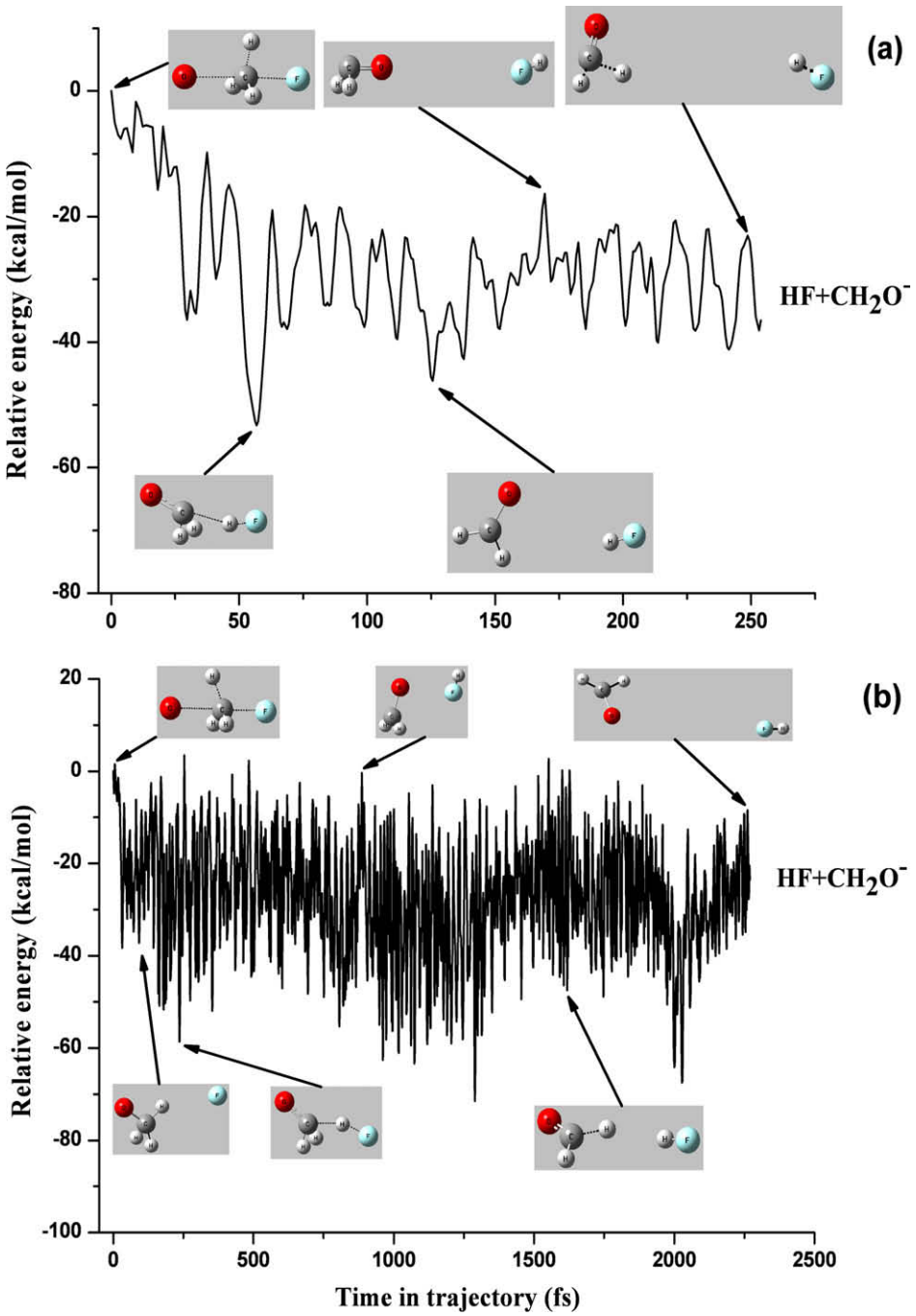

Fig. 3. Potential energy profiles initiated at the $[O\cdots CH_3\cdots F]^-$ barrier along the thermal sampling trajectories, which lead to HF and CH_2O^-. (a) The reaction process is completed with a direct and rapid dissociation within 254 fs. (b) The reaction undergoes a relatively slow process within 2270 fs, in which a $HF\cdots CH_2O^-$ intermediate complex is formed for a period of time. Molecular geometries of several typical reaction complexes are shown along these two trajectories as well.

such as $HF + CO^- + H_2$, is also due to the strong coupling of the transition vector with other vibrational modes and the efficient IVR. In summary, the coupling between the transition vector and other vibrational modes is the most significant factor to determine the dominant dynamic reaction pathways.

3.4. Dynamic reaction pathways revealed by the BOMD simulations for the H abstraction and H_2O production reaction channels

As suggested in the previous theoretical calculation [7], the H abstraction and H_2O production reaction channels undergo the same intermediate complex of $O^-\cdots HCH_2F$ and the subsequent barrier of $[O\cdots H\cdots CH_2F]^-$. Therefore, our dynamic trajectory calculations are chosen logically to initiate at this barrier. Starting from the $[O\cdots H\cdots CH_2F]^-$ barrier, a total of 61 trajectories have been calculated via the BOMD simulations with the thermal sampling at 300 K, and the trajectories with SCF convergence problems have been discarded. As mentioned in the section of computational methods, the total energies of four trajectories drift beyond 2 kcal/mol, and these four trajectories are excluded in the following discussion. Among the rest 57 trajectories, 35 of them lead to OH^- and CH_2F as products, six of them result in $H_2O + CHF^-$, two trajectories correspond to $CH_2OH + F^-$, and 14 trajectories do not meet the stopping criteria within 5000 steps. These 14 trajectories

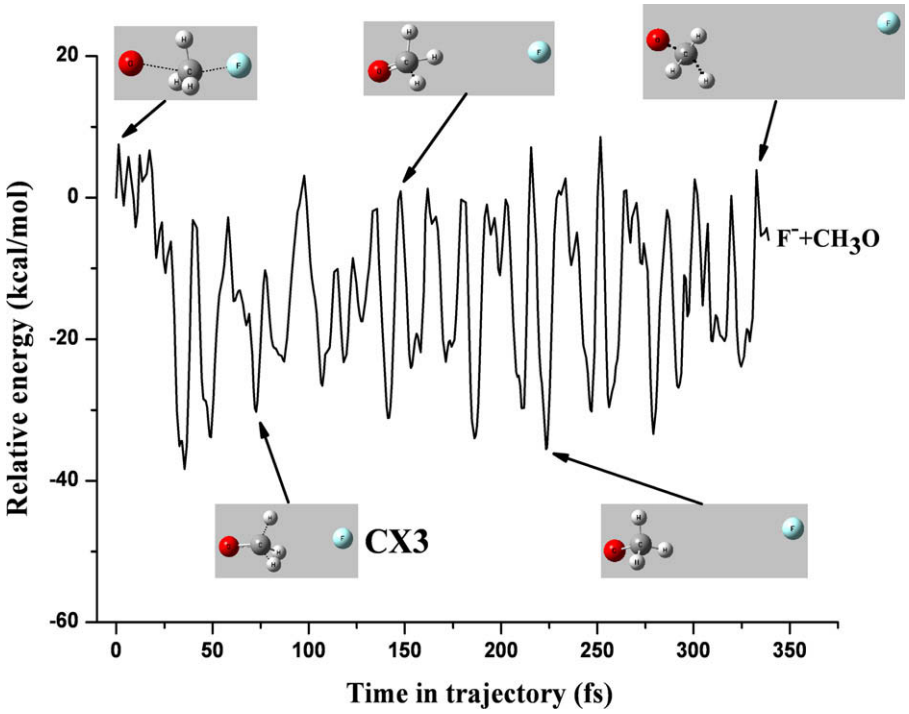

Fig. 4. Potential energy profile initiated at the $[O\cdots CH_3\cdots F]^-$ barrier along the thermal sampling trajectory, which leads to the S_N2 reaction products of F^- and CH_3O within 339 fs. Molecular structures of several key reaction complexes are exhibited along this trajectory as well.

will mostly lead to $OH^- + CH_2F$ or $H_2O + CHF^-$ with additional steps. According to the expensive computational cost and the convergence difficulty of the SCF procedure, we have not performed more trajectory calculations for this $[O\cdots H\cdots CH_2F]^-$ barrier. However, we still can draw a primary conclusion that the H abstraction channel seems to be more dominant than the H_2O production channel, which agrees with the previous experimental results [11–13]. Since the present calculations are preliminary, more efforts should be paid to calculate more dynamic trajectories to evaluate accurate branching ratios in the future.

4. Conclusions

Here we present detailed theoretical investigations on the static and dynamic reaction pathways involved in the reaction of O^- and CH_3F. Both the IRC calculations and one-dimensional relaxed potential energy scan have been performed for the S_N2 reaction channel, and the revealed static reaction process corresponds to the $HF + CH_2O^-$ products, which are unexpected in the classical S_N2 reaction mechanism. Based on the present calculations, a reasonable description of the overall static reaction process has been concluded as that the reaction initially proceeds along the S_N2 pathway to produce a S_N2 product-like complex after passing the $[O\cdots CH_3\cdots F]^-$ barrier, and then the unstable complex undergoes along the MEP to the final products of HF and CH_2O^-.

Moreover, two major types of dynamic reaction pathways initiated at the $[O\cdots CH_3\cdots F]^-$ barrier have been revealed with the BOMD simulations based on the B3LYP/6-31+G(d,p) molecular structure calculations, in which the $HF + CH_2O^-$ and $F^- + CH_3O$ are suggested to be the corresponding products. Although the HF and CH_2O^- production channel seems to be more dominant than the S_N2 pathway to produce F^- and CH_3O on the basis of our trajectory calculations, the CH_2O^- has not been observed in experiments as an anionic product, which is due to the electron detachment process of the CH_2O^-. Through comparison with the reactive system of $OH^- + CH_3F$, the coupling between the transition vector and other vibrational modes is believed as the most significant factor to determine the dominant dynamic reaction pathway.

In addition, the H abstraction and H_2O production reaction channels have been also studied with the dynamic trajectory calculations initiated at the $[O\cdots H\cdots CH_2F]^-$ barrier. Although limited trajectories are calculated and the present investigations are preliminary, we still can draw a primary conclusion that the H abstraction channel is dominant, which agrees with the previous experimental results.

Acknowledgements

The financial supports from the National Natural Science Foundation of China (NSFC, Nos. 20603033, 10979042) and National Key Basic Research Special Foundation (NKBRSF, No. 2007CB815204) are gratefully acknowledged.

Appendix A. Supplementary data

Supplementary data associated with this article can be found, in the online version, at doi:10.1016/j.theochem.2010.02.008.

References

[1] J. Shu, J.J. Lin, Y.T. Lee, X. Yang, J. Chem. Phys. 113 (2000) 9678.
[2] B. Wang, H. Hou, Y. Gu, Chem. Phys. 247 (1999) 201.
[3] X. Zhou, S. Yu, J. Li, Z. Sheng, L. Zhang, X. Ma, Chem. Phys. Lett. 339 (2001) 117.
[4] J. Espinosa-García, E.L. Coitiño, A. González-Lafont, J.M. Lluch, J. Phys. Chem. A 102 (1998) 10715.
[5] Z. Havlas, A. Merkel, J. Kalcher, R. Janoschek, R. Zahradník, Chem. Phys. 127 (1988) 53.
[6] L.A. Angel, S.P. Garcia, K.M. Ervin, J. Am. Chem. Soc. 124 (2002) 336.
[7] M. Yamamoto, K. Yamashita, M. Sadakata, J. Mol. Struct. (THEOCHEM) 634 (2003) 31.
[8] L. Sun, K. Song, W.L. Hase, Science 296 (2002) 875.
[9] L. Sun, K. Song, W.L. Hase, M. Sena, J.M. Riveros, Int. J. Mass Spectrom. 227 (2003) 315.
[10] J. Lee, J.J. Grabowski, Chem. Rev. 92 (1992) 1611. and references therein.
[11] K. Tanaka, G.I. Mackay, J.D. Payzant, D.K. Bohme, Can. J. Chem. 54 (1976) 1643.

[12] J.H.J. Dawson, K.R. Jennings, J. Chem. Soc. Faraday Trans. II 72 (1976) 700.
[13] R. Peverall, R.A. Kennedy, C.A. Mayhew, P. Watts, Int. J. Mass Spectrom. Ion Process 171 (1997) 51.
[14] R.G. Gilbert, S.C. Smith, Theory of Unimolecular and Recombination Reactions, Blackwell Press, London, 1990.
[15] W.L. Hase, Science 266 (1994) 998.
[16] C. Lee, W. Yang, R.G. Parr, Phys. Rev. B 37 (1988) 785.
[17] A.D. Becke, J. Chem. Phys. 98 (1993) 5648.
[18] C. Gonzalez, H.B. Schlegel, J. Chem. Phys. 90 (1989) 2154.
[19] C. Gonzalez, H.B. Schlegel, J. Phys. Chem. 94 (1990) 5523.
[20] K. Bolton, W.L. Hase, G.H. Peslherbe, in: D.L. Thompson (Ed.), Modern Methods for Multidimensional Dynamics Computations in Chemistry, World Scientific, Singapore, 1998, pp. 143–189.
[21] H.B. Schlegel, J. Comput. Chem. 24 (2003) 1514.
[22] H.B. Schlegel, Bull. Korean Chem. Soc. 24 (2003) 837.
[23] M.J. Frisch, G.W. Trucks, H.B. Schlegel, G.E. Scuseria, M.A. Robb, J.R. Cheeseman, J.A. Montgomery Jr., T. Vreven, K.N. Kudin, J.C. Burant, J.M. Millam, S.S. Iyengar, J. Tomasi, V. Barone, B. Mennucci, M. Cossi, G. Scalmani, N. Rega, G.A. Petersson, H. Nakatsuji, M. Hada, M. Ehara, K. Toyota, R. Fukuda, J. Hasegawa, M. Ishida, T. Nakajima, Y. Honda, O. Kitao, H. Nakai, M. Klene, X. Li, J.E. Knox, H.P. Hratchian, J.B. Cross, V. Bakken, C. Adamo, J. Jaramillo, R. Gomperts, R.E. Stratmann, O. Yazyev, A.J. Austin, R. Cammi, C. Pomelli, J.W. Ochterski, P.Y. Ayala, K. Morokuma, G.A. Voth, P. Salvador, J.J. Dannenberg, V.G. Zakrzewski, S. Dapprich, A.D. Daniels, M.C. Strain, O. Farkas, D.K. Malick, A.D. Rabuck, K. Raghavachari, J.B. Foresman, J.V. Ortiz, Q. Cui, A.G. Baboul, S. Clifford, J. Cioslowski, B.B. Stefanov, G. Liu, A. Liashenko, P. Piskorz, I. Komaromi, R.L. Martin, D.J. Fox, T. Keith, M.A. Al-Laham, C.Y. Peng, A. Nanayakkara, M. Challacombe, P.M.W. Gill, B. Johnson, W. Chen, M.W. Wong, C. Gonzalez, J.A. Pople, Gaussian 03, Revision B.05, D.01, and D.02, Gaussian Inc., Wallingford, CT, 2004.
[24] G.B. Bacskay, Chem. Phys. 61 (1981) 385.
[25] J.M. Millam, V. Bakken, W. Chen, W.L. Hase, H.B. Schlegel, J. Chem. Phys. 111 (1999) 3800.
[26] V. Bakken, J.M. Millam, H.B. Schlegel, J. Chem. Phys. 111 (1999) 8773.
[27] L.A. Curtiss, P.C. Redfern, K. Raghavachari, V. Rassolov, J.A. Pople, J. Chem. Phys. 110 (1999) 4703.
[28] K. Raghavachari, G.W. Trucks, J.A. Pople, M. Head-Gordon, Chem. Phys. Lett. 157 (1989) 479.
[29] A.P. Scott, L. Radom, J. Phys. Chem. 100 (1996) 16502.
[30] W.L. Hase, in: P.v.R. Schleyer, N.L. Allinger, T. Clark, J. Gasteiger, P.A. Kollman, H.F. Scheafer III, P.R. Schreiner (Eds.), Encyclopedia of Computational Chemistry, Wiley, Chichester, UK, 1998, pp. 402–407.
[31] G.H. Peslherbe, H. Wang, W.L. Hase, Adv. Chem. Phys. 105 (1999) 171.
[32] R.S. Mulliken, J. Chem. Phys. 23 (1955) 1833.
[33] D. Townsend, S.A. Lahankar, S.K. Lee, S.D. Chambreau, A.G. Suits, X. Zhang, J. Rheinecker, L.B. Harding, J.M. Bowman, Science 306 (2004) 1158.
[34] S.A. Lahankar, V. Goncharov, F. Suits, J.D. Farnum, J.M. Bowman, A.G. Suits, Chem. Phys. 347 (2008) 288.
[35] P.L. Houston, S.H. Kable, Proc. Natl. Acad. Sci. USA 103 (2006) 16079.
[36] J.M. Gonzales, R.S. Cox III, S.T. Brown, W.D. Allen, H.F. Schaefer III, J. Phys. Chem. A 105 (2001) 11327.
[37] Y. Zhao, N. González-García, D.G. Truhlar, J. Phys. Chem. A 109 (2005) 2012.
[38] P.D. Burrow, J.A. Michejda, Chem. Phys. Lett. 42 (1976) 223.
[39] Î. Özkan, S.Y. Chu, L. Goodman, J. Chem. Phys. 63 (1975) 3195.
[40] H. Nakatsuji, K. Ohta, K. Hirao, J. Chem. Phys. 75 (1981) 2952.
[41] N.L. Ma, W.K. Li, D.P. Chong, C.Y. Ng, Chem. Phys. 179 (1994) 365.
[42] G.L. Gutsev, L. Adamowicz, J. Phys. Chem. 99 (1995) 13412.
[43] J.S. Francisco, J.W. Thoman Jr., Chem. Phys. Lett. 300 (1999) 553.
[44] W.L. Hase, J. Phys. Chem. 90 (1986) 365.
[45] T. Uzer, W.H. Miller, Phys. Rep. 199 (1991) 73.